


Research Internship

Theory and Experimental Test of Electron Spectrometers for Laser Wakefield Accelerators

Nick Sauerwein

Abstract

This reports presents the work done at Ecole Polytechnique Paris in the scope of a extracurricular four month student internship. The main focus in set on understanding how to model, design and test a electron spectrometer for Laser Wake Field Accelerators (LWFA). This work is thought to help to design a spectrometer for the CILEX experiment.

supervised by
Dr. Arnd Specka

February 17, 2017

Contents

1 Introduction

Laser Wakefield Accelerators (LWFA) might be the accelerating structure of the future. With the possibility of reaching a stronger acceleration up to a factor of 1000 compared to conventional RF cavities, these machines are able to reach very high energies in much shorter distances. Todays plasma based accelerators however are still quite unstable. In order to further optimize the performance a good understanding of the diagnostics is needed. Therefore a lot of effort is put on better understanding the optimal configurations of a spectrometer ([3], [2]) In the following report we will present a short introduction into the theory behind spectrometers (section 2) in general and discuss special kind of spectrometers that can improve the resolution of the energy measurements (section 4). At last we will study the results of an experiment testing all the different spectrometers discussed (section 5).

For the installation only objects like magnets, stages or detectors that were already in the laboratory have been used. The purpose of the setup was not to find the best possible configuration of the spectrometer, but rather to explore and understand different methods of measuring spectra of LWFAccelerated electron beams. For the spectrometer we used

Energy range	50 MeV - 200 MeV
Divergence $\sigma(x')$	(3 ± 2) mrad
Pointing fluctuations $\sigma(\bar{x'})$	(3 ± 2) mrad

Table 1: Characteristics of electron beam.

a dipole and two quadrupoles. For further information about the dipole read section 3. The quadrupoles are specified in table ??.

	Q1	Q2	Q3
Gradient	$(288 \pm 1)\,\mathrm{T\,m^{-1}}$	- $(293 \pm 1)\,\mathrm{T\,m^{-1}}$	$(140 \pm 1)\,\mathrm{T\,m^{-1}}$
Length	(10.0 ± 0.1) mm	(40.2 ± 0.1) mm	(50.4 ± 0.2) mm

Table 2: Characteristics of quadrupoles. Note that the distance between Q1 and Q2 is zero. They are part of one mechanical unit.

2 Theory of Spectrometers

A spectrometer is a device that measures the kinetic energy distribution $\rho_E(E)$ of a particle bunch. Since it is easier to measure distributions in time or space, most spectrometers make use of a dispersion. For LWFAccelerated electron bunches which are highly relativistic, it is more useful to use dispersion in transverse space. This means that somewhere in the device there is a screen which measures for each bunch a distribution $\rho_s(a, b)$. Here a and b stand for the screen coordinates. This distribution depends on the initial conditions of the particle bunch and therefore on the distribution $\rho(\lambda)$, where $\lambda \in \mathbb{R}^6$ is a coordinate in phase space. The goal of a spectrometer is to extract information about the kinetic energy distribution $\rho_E(E)$, which is defined as a projection of the $\rho(\lambda)$ distribution, i.e.

$$\rho_E(E) = \int_{\mathcal{M}_E} d\lambda \; \rho(\lambda),$$

where $\mathcal{M}_E$ in the subspace of phase space with constant energy E.

In order to understand how ρ_s and ρ_E are related, we first have to develop a method to describe the propagation of particles through accelerators (Section 2.1). Knowing the electron trajectories in the spectrometer and assuming no correlation between energy and other properties of the initial particles it is possible to find a numerical method to extract $\rho_E(E)$ (Section 2.2).

2.1 Semi-linear Model in Frenet-Serret Coordinates

The theory discussed in this section is a modified version of the conventional method to describe particle accelerators in the linear approximation ([4]). All of the formulas are expressed in relative coordinates, i.e. in the Frenet-Serret coordinates. This means

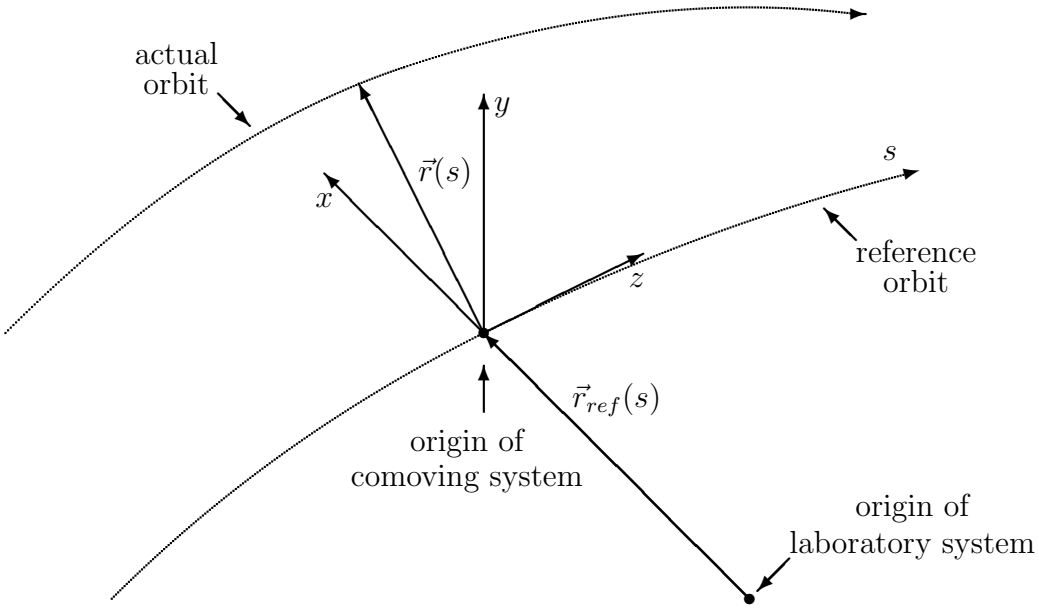

Figure 1: Local Reference System

that position and momentum of a particle is expressed relative of a reference particle with energy E_0. In a dipole this corresponds to a curvilinear coordinate system since the reference particle follows a circular path. The parameter of motion in then not the time but the traveled distance s of the reference particle. It is crucial to understand that at different reference energies E_0 the coordinates x and y correspond to different directions in the lab frame. The coordinates of the particles before the spectrometer are given by

[1]Note that normally $x' = \frac{p_x}{p_z}$. In the approximation of small transverse momenta this definition is equivalent. $D = \frac{p}{P_0} = \sqrt{1 + \frac{2\delta}{\beta_0} + \delta^2}$

x	space coordinate
$\hat{p}_x = \frac{p_x}{P_0}$	normalized momenta
$x' = \frac{p_x}{p} = \hat{p}_x/D$	slope of particle[1]
$\delta = \frac{E-E_0}{P_0}$	energy deviation[2]

Table 3: Definitions of coordinates with the respect to classical choice

$x^{(i)}$, $\hat{p}_x^{(i)}$, $y^{(i)}$, $\hat{p}_x^{(i)}$ and $z^{(i)}$. After the electron optics they will be called $x^{(f)}$, $\hat{p}_x^{(f)}$, $y^{(f)}$, $\hat{p}_x^{(f)}$ and $z^{(f)}$. Since the Hamiltonians of quadrupoles, dipoles and drifts are independent of z, the energy divination $\delta = \frac{E-E_0}{P_0} = \delta_i = \delta_f$ $(c = 1)$ remains constant throughout the lattice.

Due to electron bunches accelerated by a LWFA being very localized in space and momentum, it is a good approximation to expand the Hamiltonians up to second order in the transverse coordinates and z. In δ however the full dependence must be kept because the spectrometers is thought to be applied for accelerators with high energy spreads ($\Delta\delta \approx 0.5$). In this case we can write down the map of the lattice in the following form

$$\xi^{(f)} = \mathbf{M}(\delta)\xi^{(i)} + \mathbf{v}(\delta) \tag{2.1.1}$$

, where $\xi = [x, \hat{p}_x, y, \hat{p}_x, z, \delta]^T$, $\mathbf{M}(\delta) \in M(5, \mathbb{R})$ and $\mathbf{v}(\delta) \in \mathbb{R}^5$. In the following we will call $\mathbf{M}$ as the transport matrix and $\mathbf{v}$ as the dispersion vector. If the accelerator consist of n elements, $\mathbf{M}$ and $\mathbf{v}$ can be found by

$$\begin{aligned} \mathbf{M} &= \mathbf{M}_n \ ... \ \mathbf{M}_1 \\ \mathbf{v} &= \mathbf{v}_n + \mathbf{M}_n\mathbf{v}_{n-1} + ... + \mathbf{M}_n \ ... \ \mathbf{M}_2\mathbf{v}_1, \end{aligned}$$

where the $\mathbf{M}_i$ and $\mathbf{v}_i$ are of the specific elements (Appendix 7.1). Sometimes it is convenient to define a multiplication[3] of $\text{Element}_1 = (\mathbf{M}_1, \mathbf{v}_1)$ and $\text{Element}_2 = (\mathbf{M}_2, \mathbf{v}_2)$ as

$$\text{Element}_2 * \text{Element}_1 = (\mathbf{M}_2 \ \mathbf{M}_1, \mathbf{v}_2 + \mathbf{M}_2\mathbf{v}_1). \tag{2.1.2}$$

An beamline matrix can that be written as a multiplication of elements. Note that this approximation is only valid, if all components of $\mathbf{v}$ except z are small. In $\mathbf{v}_{di}$ this will lead to the condition

$$\frac{D-1}{k_0}\,(1 - \cos(\omega L)) \ll 1.$$

This above condition will fix the range of validity for the model.

2.1.1 Screen Coordinates

The screen is a projection of the particles bunch on a 2D surface. Here we will only consider planar screens which are tilted about an angle φ to the laboratory x axis. The coordinates of particles on the screen are describe by (a, b), where the a direction lies in the x-z plane and b is parallel to y. Since the introduced theory makes use of curvilinear

[2] In many textbooks δ is defined as the momentum deviation. For highly relativistic particles (LWFA) the difference in the definitions becomes less relevant.

[3] This definition is analogous to the multiplication of two elements of the affine group.

coordinate systems which are depended on an energy E_0 of a reference particle, quantities like distances between elements or also the screen angle φ_{E_0} become E_0 dependent. Using trigonometry one can express a and b as a function of the final coordinates of the particles, i.e.

$$a = \frac{x^{(f)} - z^{(f)}\ x'^{(f)}}{\cos(\varphi_{E_0}) - x'^{(f)} \sin(\varphi_{E_0})} \approx \frac{x^{(f)}}{\cos(\varphi_{E_0})} \tag{2.1.3}$$

$$b = y^{(f)} + y'^{(f)} \left(a \sin(\varphi_{E_0}) - z^{(f)}\right) \approx y^{(f)}. \tag{2.1.4}$$

2.1.2 Calibration Curve and Error on Energy Measurement

For all the considered cases we amuse a dispersion in the a direction on the screen. As long as the dispersion follows a line (linear case) one can always change coordinates (rotate the spectrometer) to reach this condition. The calibration curve $\delta(a)$ can be found by inverting the dispersion function $a(\delta)$ which is defined by

$$a(\delta) = a\Big|_{\xi^{(i)}=0} = \frac{\mathbf{v}_x - \mathbf{v}_z \mathbf{v}_{\hat{p}_x}/D}{\cos(\varphi_{E_0}) - \mathbf{v}_{\hat{p}_x}/D \sin(\varphi_{E_0})}.$$

In section 4.2 we will discuss a dispersion where a mean deviation of the beam $x' \neq 0$ is crucial. For this case the same definition of the here derived qualities can be used, but the accelerator map must be modified by a 0^{th} element of the form ($\mathbf{M}_0 = \mathbb{1}$, $\mathbf{v} = x' D\ \vec{e}_2$). The calibration curve can be derived analytically by expanding the dispersion function $a(\delta)$ up to second order in δ and then inverting. This result will however only be valid for a small energy divination δ. Since the model so far doesn't make use of expansions in δ, the calibration curve should rather be calculated by numerical inversion under the condition that $x^{(f)} \ll 1$ and $\hat{p}_x^{(f)} \ll 1$. In case of a non-vanishing $\hat{p}_x^{(i)}$ the energy becomes in general a function of a and $\hat{p}_x^{(i)}$, $\delta(a, \hat{p}_x^{(i)})$. If $\sigma(x')$ is the standard deviation of the initial divergence of the beam, the error on the energy measurement is given by

$$\Delta\delta = \frac{\partial \delta(a, \hat{p}_x^{(i)})}{\partial \hat{p}_x^{(i)}}\bigg|_{\hat{p}_x^{(i)}=0} D\ \sigma(x'). \tag{2.1.5}$$

Since a is fixed in the above equation, the value of this derivative can be found implicitly

$$\begin{aligned} 0 = \frac{\mathrm{d}a}{\mathrm{d}\hat{p}_x^{(i)}} &= \frac{\partial a}{\partial \hat{p}_x^{(i)}} + \frac{\partial a}{\partial \delta} \frac{\partial \delta}{\partial \hat{p}_x^{(i)}} \\ \implies \frac{\partial \delta}{\partial \hat{p}_x^{(i)}}\bigg|_a &= -\left(\frac{\partial a}{\partial \hat{p}_x^{(i)}}\right) \Big/ \left(\frac{\partial a}{\partial \delta}\right). \end{aligned}$$

2.1.3 Focusing Conditions

For later analysis it is important to define different focus conditions. Firstly, we have the point-to-point (stigmatic) focus, secondly two different point-to-line focuses (a or b stigmatic) and thirdly the collimated beam condition.

Stigmatic Focus Condition Point-to-point focus means that the position of the electrons (a, b) is for a specific energy δ_0 independent of the initial momenta $\hat{p}_x$ and $\hat{p}_y$. In the introduced formalism this condition corresponds to

$$\left.\frac{\partial a}{\partial \hat{p}_x^{(i)}}\right|_{\xi^{(i)}=0,\ \delta=\delta_0} = 0 \implies \mathbf{M}_{12}(\delta) = 0 \tag{2.1.6}$$

$$\left.\frac{\partial b}{\partial \hat{p}_x^{(i)}}\right|_{\xi^{(i)}=0,\ \delta=\delta_0} = 0 \implies \mathbf{M}_{34}(\delta) = 0 \tag{2.1.7}$$

Line Focus Conditions Line focus means that the position of the electrons is for a specific energy δ_0 independent of the initial momentum, either a independent of $\hat{p}_x^{(i)}$ or b independent of $\hat{p}_y^{(i)}$. In the other direction divergence of the beam is zero. In the introduced formalism this condition (a line) corresponds to

$$\left.\frac{\partial a}{\partial \hat{p}_x^{(i)}}\right|_{\xi^{(i)}=0,\ \delta=\delta_0} = 0 \implies \mathbf{M}_{12}(\delta) = 0$$

$$\left.\frac{\partial \hat{p}_x^{(f)}}{\partial \hat{p}_x^{(i)}}\right|_{\xi^{(i)}=0,\ \delta=\delta_0} = 0 \implies \mathbf{M}_{33}(\delta) = 0$$

The for y this condition is analog.

Collimated Beam Condition The beam is called collimated if $\hat{p}_x^{(f)}$ and $\hat{p}_y^{(f)}$ is zero for a specific energy δ_0 In the introduced formalism this condition corresponds to

$$\left.\frac{\partial \hat{p}_x^{(f)}}{\partial \hat{p}_x^{(i)}}\right|_{\xi^{(i)}=0,\ \delta=\delta_0} = 0 \implies \mathbf{M}_{11}(\delta) = 0$$

$$\left.\frac{\partial \hat{p}_y^{(f)}}{\partial \hat{p}_x^{(i)}}\right|_{\xi^{(i)}=0,\ \delta=\delta_0} = 0 \implies \mathbf{M}_{33}(\delta) = 0$$

General Astigmatic Focus Condition This condition is similar to stigmatic focus, but here the beam is focused in x and y for different energies δ_{0x} and δ_{0y}. In the introduced formalism this condition corresponds to

$$\left.\frac{\partial a}{\partial \hat{p}_x^{(i)}}\right|_{\xi^{(i)}=0,\ \delta=\delta_{0x}} = 0 \implies \mathbf{M}_{12}(\delta_{0x}) = 0$$

$$\left.\frac{\partial b}{\partial \hat{p}_x^{(i)}}\right|_{\xi^{(i)}=0,\ \delta=\delta_{0y}} = 0 \implies \mathbf{M}_{34}(\delta_{0y}) = 0$$

2.1.4 Optimal Energy Resolution around E_0

In order to have maximal energy resolution on the screen the final coordinate a must only be dependent on the energy δ of the particle and not on its initial transverse momentum $\hat{p}_x^{(i)}$ in the dispersive plane

$$\frac{\partial a}{\partial \hat{p}_x^{(i)}}(\delta) = 0 \quad \forall \delta \in\ ]-\delta_{min}, \infty[.$$

This condition corresponds to a perfect global energy resolution. It can be solved by a Taylor expansion of δ around 0. The 0^{th} order leads to the x focusing condition in equation 2.1.6. From the 1^{st} order it can be inferred that

$$\begin{aligned} &\frac{\partial^2 a}{\partial \hat{p}_x^{(i)} \partial \delta}\bigg|_{\xi^{(i)}=0,\ \delta=0} = 0 \\ &\implies \tan(\varphi_{E_0}) = \frac{\mathbf{M}'_{12} - \mathbf{v}'_z \mathbf{M}_{22} - \mathbf{v}'_{\hat{p}_x} \mathbf{M}_{52}}{\mathbf{v}'_x \mathbf{M}_{22}}\bigg|_{\delta=0}. \end{aligned} \tag{2.1.8}$$

Here the notation $Q' = \frac{\partial Q}{\partial \delta}$ has been applied.

2.2 Algorithm for Reconstruction of Energy Distribution

Let us fist calculate the projected distribution of particles on the screen by assuming a fixed distribution in the transverse momenta. We will also assume the initial positions x,y and z of the particles to be zero. This is a good approximation if the resolution on the screen is bigger than the image of the bunch after magnification of the optics in the spectrometer. The distribution of electron in the bunch at the source is assumed to be

$$\rho(\xi, \delta) = \hat{\delta}(x)\hat{\delta}(y)\hat{\delta}(z)\rho_\perp(\hat{p}_x, \hat{p}_y; \delta)\rho_\delta(\delta) \tag{2.2.1}$$

where $\hat{\delta}(x)$ is the Dirac delta function. The projected distribution on the screen $\rho_s(a, b)$ can be obtained by integrating over $\mathcal{M}_{ab} = \{(\xi, \delta) \in \mathbb{R}^5 \times]\delta_{min}, \infty[\ |a = a(\xi, \delta),\ b = b(\xi, \delta)\}$, i.e. the inverse image of the accelerator when keeping (a, b) fixed. δ_{min} is the minimal accepted energy of the spectrometer[4].

$$\rho_s(a, b) = \int_{\mathcal{M}_{ab}} d\lambda\ \rho(\xi, \delta) \tag{2.2.2}$$

In the following we will evaluate this integral by change on coordinates such that $\mathcal{M}_{ab} = a \times b \times \mathbb{R}^4$. The change of variable will then be given by

$$\phi(\xi, \delta) = (a, b, x, y, z, \delta) \underbrace{=}_{eq.2.1.3(\text{1st order})} (x_f/\cos(\varphi_{E_0}), y_f, x, y, z, \delta) \tag{2.2.3}$$

where x_f and y_f have been expressed to first order in the screen coordinates.

$$\begin{aligned} \rho_s(a, b) &= \int_{\delta_{min}}^{\infty} d\delta \int_{\mathbb{R}^3} dx\ dy\ dz\ |J_{\phi^{-1}}|\ \hat{\delta}(x)\hat{\delta}(y)\hat{\delta}(z)\ \rho_\perp(\hat{p}_x, \hat{p}_y; \delta)\ \rho_\delta(\delta) \\ &= \int_{\delta_{min}}^{\infty} d\delta\ |J_{\phi^{-1}}|\ \rho_\perp(\phi_2^{-1}, \phi_4^{-1}; \delta)\ \rho_\delta(\delta). \end{aligned} \tag{2.2.4}$$

The functions ϕ_2^{-1}, ϕ_4^{-1} and $|J_{\phi^{-1}}|$ are given by

$$\begin{aligned} \phi_2^{-1} &= \frac{a\cos(\varphi_{E_0}) - \mathbf{v}_x}{\mathbf{M}_{12}} \\ \phi_4^{-1} &= \frac{b - \mathbf{v}_y}{\mathbf{M}_{34}} \\ |J_{\phi^{-1}}| &= \left|\frac{\cos(\varphi_{E_0})}{\mathbf{M}_{12}\mathbf{M}_{34}}\right|. \end{aligned}$$

[4] In a spectrometer which uses a dipole it can be defined through $R_{min} = L_{di}$, where R_{min} is the curvature radius corresponding to δ_{min}

2.2.1 General Solution using Numerical Fredholm Equation Solver

Introducing $K(a,b;\delta) = |J_{\phi^{-1}}|\ \rho_\perp(\phi_2^{-1}, \phi_4^{-1})$ the problem reduces to

$$\rho_s(a,b) = \int_{\delta_{min}}^{\infty} d\delta\ K(a,b;\delta)\ \rho_\delta(\delta).$$

When we assume a angular distribution, the function K is known. The next step is to find a numerical algorithm that can invert this Fredholm equation of first kind. Following the ideas of Richard J. Hanson we will approximate the integral by as sum over discrete values. We introduce the multi-index $\alpha = (i,j) \in \{1 \dots m\} \otimes \{1 \dots l\}$ for the discretization in (a,b) and $k \in \{1 \dots n\}$ for δ:

$$\rho_{s\alpha} = \sum_k \omega_k\ K_{\alpha k}\ \rho_{\delta k}.$$

Here ω_k are the weights for the numerical integration. Introducing $A_{\alpha k} = w_k\ K_{\alpha k}$ the problem becomes a linear least-squares of the following form

$$\rho_\delta = \min_{x \in \mathbb{R}^n} \|Ax - \rho_s\|^2_{\mathbb{R}^{m \times l}},$$

which can be solved efficiently using singular value decomposition (SVD). Since the density on the screen ρ_s is a measured quantity it contains errors. The naive way to solve the above problem is not at all stable and would result in false results. We will a apply the regularization method in combination with SVD like explained by L. Dykes and L. Reichel (ref). Let us therefore introduce the regularization matrices $L^{(i)}$ which correspond to the discretized i^{th} derivatives.

$$L^{(0)} = \mathbb{1}$$

$$L^{(1)} = \begin{bmatrix} 1 & -1 & 0 & \dots & 0 \\ 0 & 1 & -1 & \ddots & \vdots \\ \vdots & \ddots & \ddots & \ddots & 0 \\ 0 & \dots & 0 & 1 & -1 \end{bmatrix}$$

$$L^{(2)} = \begin{bmatrix} -1 & 2 & -1 & 0 & \dots & 0 \\ 0 & 1 & 2 & -1 & \ddots & \vdots \\ \vdots & \ddots & \ddots & \ddots & \ddots & 0 \\ 0 & \dots & 0 & 1 & 2 & 1 \end{bmatrix}$$

After regularization the problem reads

$$\rho_\delta = \min_{x \in \mathbb{R}^n} \|Ax - \rho_s\|^2_{\mathbb{R}^{m \times l}} + \sum_{i=0}^{n-1} \mu_i \left\| L^{(i)} x \right\|^2_{\mathbb{R}^{(m \times l) - i}}. \tag{2.2.5}$$

For the case of energy reconstruction we will only consider the regularization of second order (i = 2). This order is the most effective to filter out fast oscillations. As explained in Chapter 2.3 of [1] one can bring 2.2.5 if only one $\mu_i \neq 0$ to the standard form

$$\hat{\rho_\delta} = \min_{\hat{x}} \left\| \hat{A}\hat{x} - \hat{\rho_s} \right\|^2 + \mu \|\hat{x}\|^2.$$

Such a regression is called Ridge and can be solved using `sklearn` in `python`. The parameter μ can be estimated with the Generalized Cross Validation (GCV). The correspond function in `python` is called `RidgeCV`.

2.2.2 Vertical Projection Method

This method makes the assumption that the transverse beam profile is a Dirac delta function $\hat{\delta}$, i.e.

$$\rho_{\perp}(\hat{p}_x, \hat{p}_y; \delta) = \hat{\delta}(\hat{p}_x)\hat{\delta}(\hat{p}_y).$$

Plugging this in eq. 2.2.4 and integrating over b yields

$$\begin{aligned}\int_{-\infty}^{\infty} db\ \rho_s(a,b) &= \int_{-\infty}^{\infty} db \int_{\delta_{min}}^{\infty} d\delta\ |J_{\phi^{-1}}|\ \hat{\delta}(\phi_2^{-1})\ \hat{\delta}(\phi_4^{-1})\ \rho_{\delta}(\delta) \\ &= \frac{\partial \delta(a)}{\partial a}\ \rho_{\delta}(\delta(a))\end{aligned}$$

where we defined $\delta(a)$ as the inverse of $a(\delta) = \mathbf{v}_x/\cos(\varphi_{E_0})$. This formula gives a simple and numerically stable recipe to calculate the energy distribution ρ_{δ}. It however totally neglects the widening of electron beams due to divergence.

3 Modeling of Permanent Dipole Magnet

In the APPENDIX (7.1) the result for the dipole map in the semi-linear model (Section 2.1) is given. For later experiments with the spectrometer we need to find the model which describes the real magnet best. In order to fit the parameters, like length L_{di} and field strength b a field map of the real dipole magnet has been measured using a Hall probe mounted on a 3D translation stage. This information was then fed into a field map tracking software (Section 7.4.2). Using the trajectories of the particles it is possible to calculate the real world linear matrix and find the best parameters for the model to fit. In our analysis we focused on two different models for the dipole. Firstly the standard Single Dipole Hard-edge Model which assumes that the dipole has no far reaching fringe field. Secondly the Triple Dipole Hard-edge Model which includes the far reaching fringe field by modeling it as a separate weaker dipole.

3.1 Real Field of Dipole Magnet

In the center of a dipole bending magnet the field[5] B_z is constant (Figure 2). The field decreases rapidly at the boundaries of the magnet (x =0 and 50 mm). Because of $\nabla \cdot B = 0$ a decrease of B_z along z will result in an increase of B_x along x. The strong B_x fields at the boundaries load to a focusing/defocusing of the bunch at the exit of the dipole in the vertical/horizontal plane assuming that the reference trajectories are perpendicular on the entrance of the dipole. In figure 2 it is visible that the B_z field extents far out the magnet. Outside it is however of opposite direction as inside. This can be explained by the fact that the soft iron yoke is undersized. Then the yoke becomes saturated and the field escapes outside the magnet.

[5] In this section we will use a different coordinate system. z is the main field direction and x is the propagation direction of the electrons through the dipole.

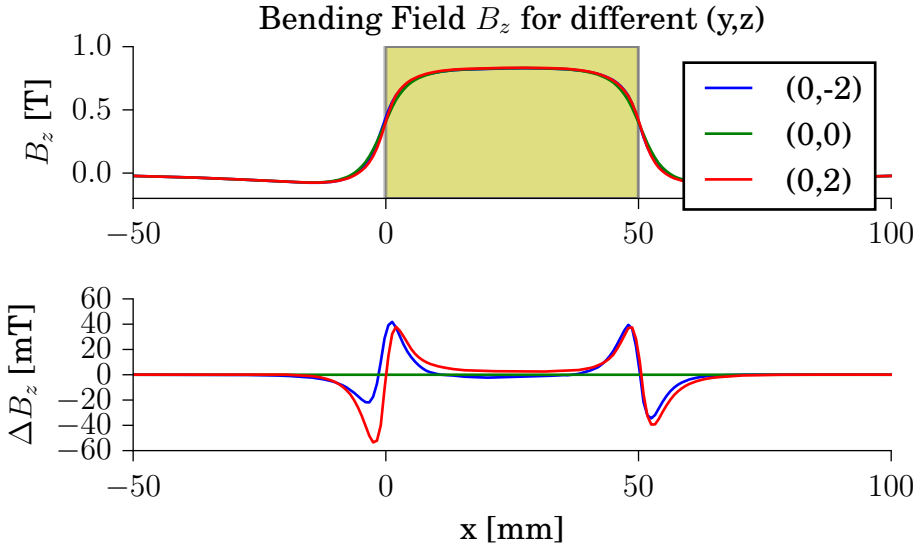

Figure 2: This plot has been generated from a field map of the magnet used in the experiment (Section 5). $\Delta B_z = B_z - B_z|_{z=0,\ y=0}$ is the variation of B_z which respect to infinite energy particle trajectory.

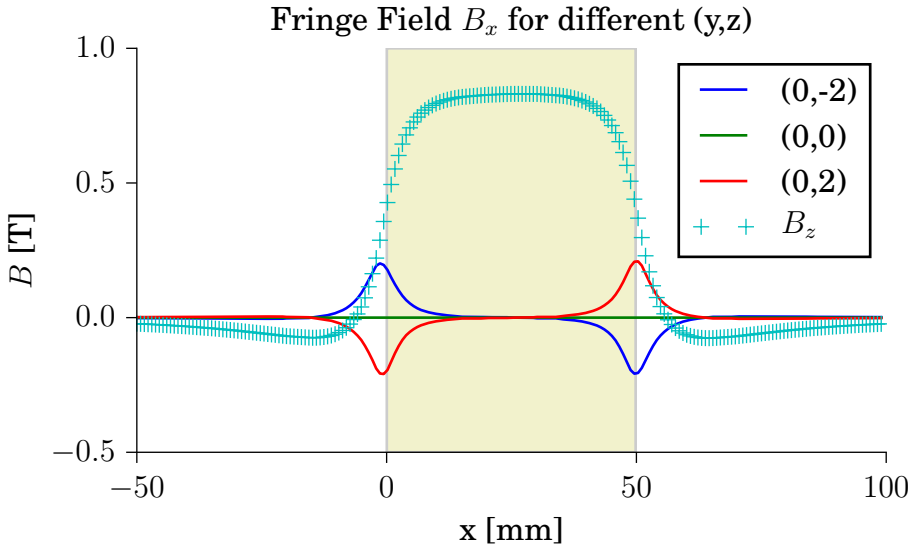

Figure 3: This plot has been generated from a field map of the magnet used in the experiment (Section 5).

3.2 Extraction of Semi-Linear Map form Magnetic Field Map

From a field map one can calculate all particles trajectories using numerical integration methods (`scipy.integrate.odeint`). So for each initial condition $(\xi^{(i)}, \delta)$ the final position (after distance s of the reference particle) in the Frenet-Serret coordinates $\Psi_s^\delta(\xi^{(i)}) = \xi^{(f)}$ can be calculated. Here we will call Ψ_s^δ the numerical propagator over the distance s. By construction of the coordinate system we get $\Psi_s^0(0) = 0$ and $\Psi_0^\delta = \mathbb{1}$. The

transfer matrix $\mathbf{M}$ and vector $\mathbf{v}$ can then be estimated component wise as

$$\mathbf{M}_{ij}(\delta) = \frac{\Psi_s^\delta(0,...,0,\overbrace{\epsilon}^{j^{\text{th}}\text{ entry}},0,...,0)_i - \Psi_s^\delta(0)_i}{\epsilon}$$
$$\mathbf{v}_i(\delta) = \Psi_s^\delta(0)_i$$

for ϵ small.

3.3 Different Models for Dipole Magnets

In this section two different models for a permanent magnet dipole are described. Both models rely on the semi-linear model described in section 2.1.

Single Dipole Hard-edge Model (SDH) This is the classical way to model a dipole magnet. Here we would take the matrix of the dipole $\mathbf{M}_{di}$ and multiply it from left with the fringe field focusing matrix $\mathbf{M}_f$ where we use the bending angle ϑ_{E_0} equals the exiting angle. Equation wise this means

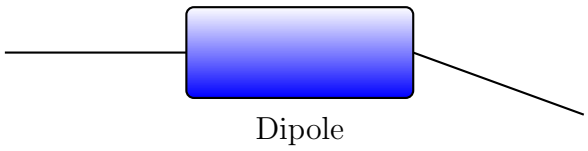

Figure 4: Schematic drawing of Single Dipole Hard-edge Model

$$\text{Model}_1(s, d_1, B) = \text{Drift}(s - s_{di} - d_1) * \text{Fringe}(\vartheta_{E_0}) * \text{Dipole}(L_{di}, B) * \text{Drift}(d_1).$$

Triple Dipole Hard-edge Model (TDH) This model has been developed in order to give a better description of the dipole. The long reaching fringe field (Figure 2) here have been modeled as two additional weaker dipole with opposite polarization.

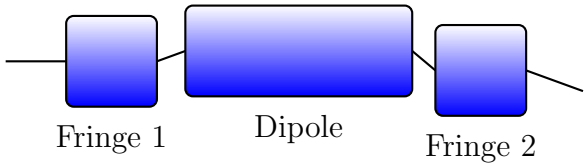

Figure 5: Schematic drawing of Triple Dipole Hard-edge Model

$$\begin{aligned}\text{Model}_2(s, d_1, B) = \text{Drift}(s - s_{di_1} - s_{di_2} - s_{di_3} - d_1 + d_2 + d_3) * \text{Fringe}(\vartheta_{1E_0} + \vartheta_{2E_0} + \vartheta_{3E_0}) \\ * \text{Dipole}(L_{di_3}, B_3) * \text{Fringe}(-\vartheta_{1E_0} - \vartheta_{2E_0}) * \text{Drift}(d_3) \\ * \text{Fringe}(\vartheta_{1E_0} + \vartheta_{2E_0}) * \text{Dipole}(L_{di_2}, B_3) * \text{Fringe}(-\vartheta_{1E_0}) \\ * \text{Drift}(d_2) * \text{Fringe}(\vartheta_{1E_0}) * \text{Dipole}(L_{di_1}, B_1) * \text{Drift}(d_1)\end{aligned}$$

Note that since $B_1,\ B_3 < 0$ also $\vartheta_{1E_0},\ \vartheta_{3E_0} < 0$.

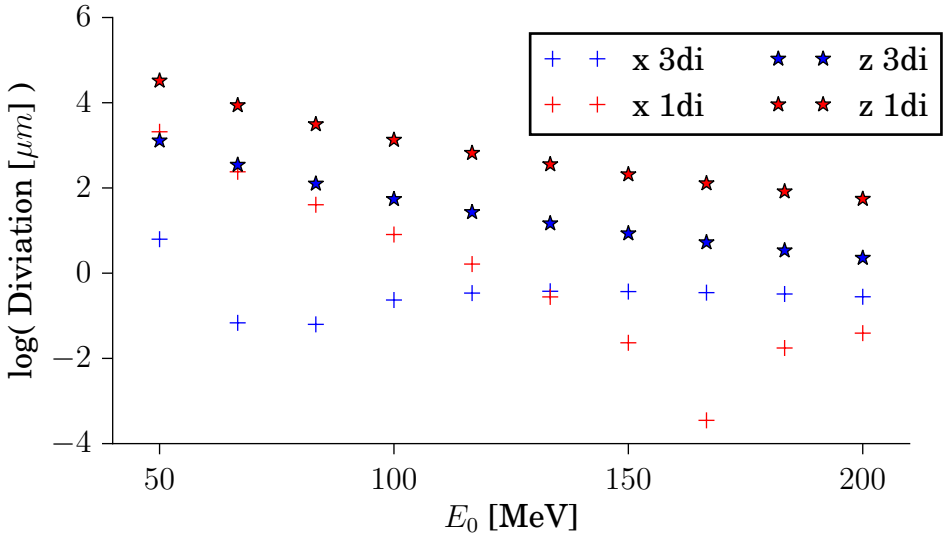

Figure 6: Here the two models are compared to a tracking though the fieldmaps of the dipole. 3di and 1di stands for the different models for the dipole. Only the deviations of the reference trajectories with respect to the fieldmap trajectories have been considered.

Results for Models of Real Magnet Figure 6 shows the deviation of the reference trajectories of the models with the trajectories calculated by numerical integration. It indicates that using the Triple Dipole Hard-edge Model (3di) an improvement of 2 orders of magnitude can be achieved in the quality of the model. Figure 6 however makes no statement the quality of the models with respect to the electron optics. In order to get the full picture one should also look at the transfer matrices or vectors. An example of the matrices is shown in table 5. Based on these outputs no significant improvement in the precision of the model has been observed. We therefore come to the conclusion that the SDM is sufficient to describe the dynamics of the electrons.

Table 4: Results for parameters of models

(a) SDM

$$B = 0.72\,\mathrm{T}$$
$$L_{di} = 50\,\mathrm{mm}$$
$$d_1 = 0\,\mathrm{mm}$$

(b) TDM

$$(B_1,\ B_2,\ B_3) = (-0.11\,\mathrm{T},\ 0.82\,\mathrm{T},\ -0.056\,\mathrm{T})$$
$$(L_{di_1},\ L_{di_2},\ L_{di_3}) = (10\,\mathrm{mm},\ 47\,\mathrm{mm},\ 26\,\mathrm{mm})$$
$$(d_1,\ d_2,\ d_3) = (15\,\mathrm{mm},\ 26\,\mathrm{mm},\ 12\,\mathrm{mm})$$

	M	**v** [mm, mrad]
Tracking	$\begin{bmatrix} 0.99056 & 0.115 & 0.00437 & -0.00115 & 0.01582 \\ -0.02674 & 1.00475 & 0.06638 & 0.00292 & -0.00211 \\ 0. & 0. & 1.00789 & 0.11603 & 0. \\ 0. & 0. & 0.20433 & 1.0157 & 0. \\ -0.10778 & -0.00769 & -0.00053 & 0.00002 & 1.00025 \end{bmatrix}$	$\begin{bmatrix} 1.8767 \\ 32.55176 \\ 0. \\ 0. \\ -0.03313 \end{bmatrix}$
SDM	$\begin{bmatrix} 0.9944 & 0.11532 & 0. & 0. & 0. \\ -0.02855 & 1.00232 & 0. & 0. & 0. \\ 0. & 0. & 1.00793 & 0.11607 & 0. \\ 0. & 0. & 0.20612 & 1.01587 & 0. \\ -0.108 & -0.00672 & 0. & 0. & 1. \end{bmatrix}$	$\begin{bmatrix} 1.87226 \\ 32.42336 \\ 0. \\ 0. \\ -0.03213 \end{bmatrix}$
TDM	$\begin{bmatrix} 0.99405 & 0.11532 & 0. & 0. & 0. \\ -0.0347 & 1.00196 & 0. & 0. & 0. \\ 0. & 0. & 1.00843 & 0.11611 & 0. \\ 0. & 0. & 0.20366 & 1.01509 & 0. \\ -0.10793 & -0.0067 & 0. & 0. & 1. \end{bmatrix}$	$\begin{bmatrix} 1.87249 \\ 32.3806 \\ 0. \\ 0. \\ -0.02409 \end{bmatrix}$

Table 5: Example matrices for different models ($E_0 = 100\,\mathrm{MeV}, \delta = 0.3$)

4 Discussion of Specific Spectrometer Configurations

4.1 Dipole Spectrometer

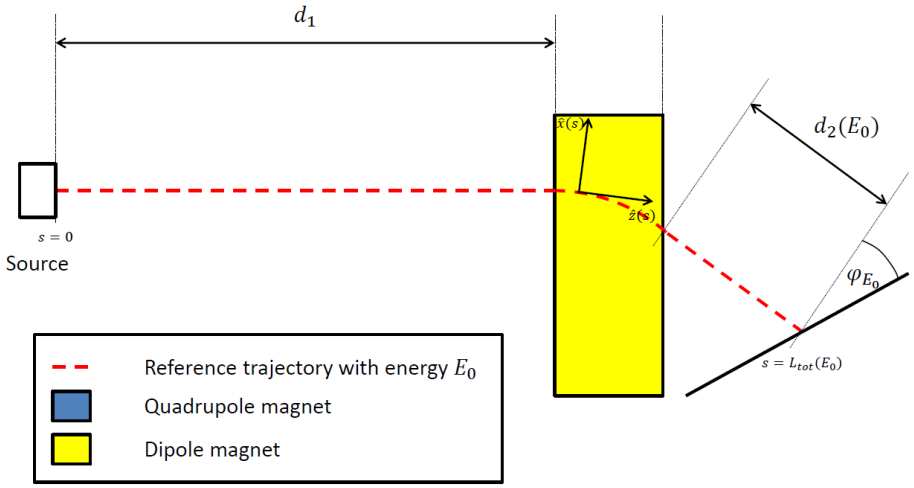

Figure 7: Layout of the dipole spectrometer beamline.

Using a dipole magnet provides a very simple method to measure the distribution of kinetic energy. The maximal energy resolution of such a spectrometer is mainly limited by the pointing fluctuations of the electron beam. In order to calibrate the scale, the infinite energy point (point on screen of undeflected electron bunch) has to be determined. This

requires moving the dipole out of the beam trajectory. Since deformations in the laser wavefront (cite ...) or transversal density gradients in the plasma can lead to mismatch between the laser and electron axis, the procedure of finding the calibration point has to be redone when parameters of the laser or plasma source are changed. In section 2.1.4 the conditions for perfect resolution around an energy E_0 have been derived. With a dipole only however it is for high energies not possible to reach these conditions because the effects of fringe field focusing are to small. Therefore this configuration of spectrometer has a maximal possible resolution. In the following part we are going to discuss the optimal energy resolution when we assume a homogeneous dipole and neglect fringe field focusing effects.

4.1.1 Optimal Resolution in Ideal Dipole Approximation

Here we will determine the best possible resolution assuming rectangular dipole with field B and a length of L. The distance between the electron source and the dipole is d_1. The screen is placed parallel to the dipole at a distance d_2. An electron with divergence $[x'] = \text{rad}$ to an axis perpendicular to the dipole entry will have

$$a = d_1\, x' - R + \frac{1}{\sqrt{R^2 - L^2}} \left[R^2 - L^2 + L\, R\, x' - d_2\, L + d_2\, R\, x' \, \frac{R^2}{R^2 - L^2} \right]$$

as the position on the screen. Here $R = \dfrac{eP}{B}$ is the radius of the electron with momentum P in a homogeneous magnetic field B. Note that $a = 0$ corresponds to the point on screen of an electron with infinite energy and $x' = 0$. The resolution can be calculated using formula 2.1.5. Hence

$$\Delta E/E = A(d_1, d_2, L, R)\ \sigma(x')$$

where A is given by

$$A(d_1, d_2, L, R) = \frac{d_1 + \dfrac{R}{R^2 - L^2} \left[L + d_2 \dfrac{R^2}{R^2 - L^2} \right]}{\dfrac{R^2}{\sqrt{R^2 - L^2}} \left[1 + \frac{d_2\, L}{R^2 - L^2} \right] - R}.$$

The optimal resolution can be found by taking the limit $d_2 \to \infty$ which results in

$$\lim_{d_2 \to \infty} A(d_1, d_2, L, R) = \frac{R}{L}. \tag{4.1.1}$$

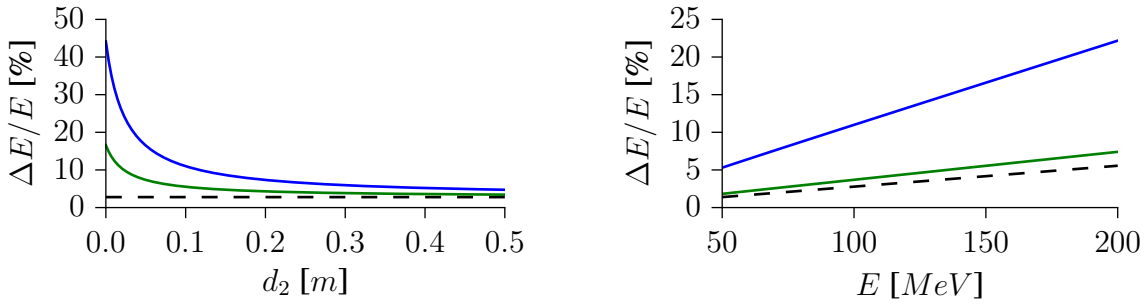

(a) (b)

Figure 8: Plots of the resolution $\Delta E/E$ with respect to (8a) d_2 at fixed $E = 100\,\text{MeV}$ and (8b) E at fixed distances d_2 (0.1 m (blue), 0.35 m (green)). In both plots d_1 is fixed (0.35 m (blue), 0.1 m (green)). The L_{di} and B used correspond to the dipole used in the experiments (section 3.1).

4.2 Quadrupole Triplet Spectrometer

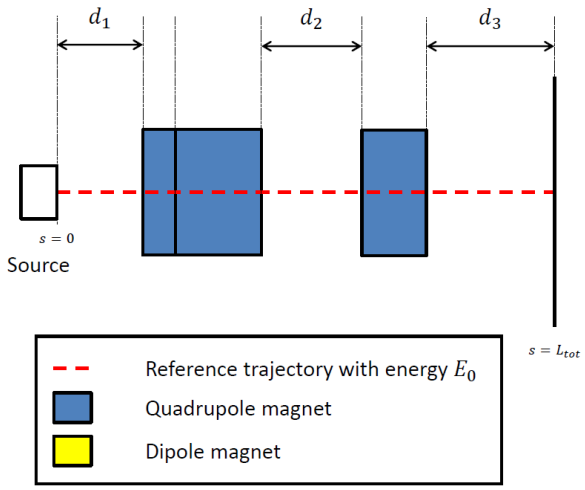

Figure 9: Layout of quadrupole triplet spectrometer beamline.

Let us assume a source which is aligned with a quadrupole triplet as shown in image 9. The distances d_1, d_2 and d_3 are tuned in such a way that the conditions in section 2.1.4 are satisfied for E_0. The screen however is chosen to be perpendicular to the quadrupole axis. If the electron bunches exit the source under an mean angle $\bar{x'} \neq 0$, they will be dispersed on the screen. The electrons of energy E_0 will by construction be mapped to $a = 0$ on the screen. Electrons with higher/lower energies however will be under/over-focused on the screen. This effect introduces a dispersion in a which is a result of the chromaticity of the quadrupole triplet.

4.2.1 Resolution

As described in section 2.1.2 one can define the calibration curve $a(\delta)$ and the error of the spectrometer $\Delta E/E$. Since a quadrupole spectrometer is tunable in E_0 we can give many

resolution curves corresponding to the different optimal configurations. The dispersion curve as well as the error are in the applied approximation linearly depended on the mean deviation x'.

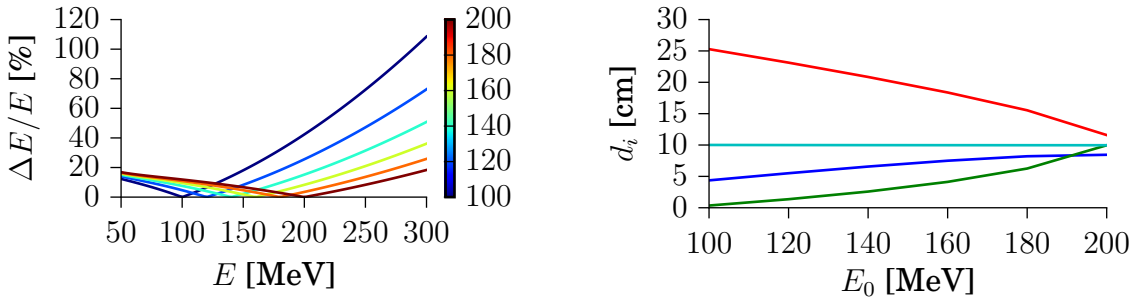

Figure 10: d_1 (blue), d_2 (green), d_3 (red), d_4 (cyan). The mean deviation $\bar{x'}$ of the beam is for all plots chosen to be 10 mrad. The divergence of the beam $\sigma(x')$ is taken to be 3 mrad.

4.3 Quadrupole Triplet and Dipole Spectrometer

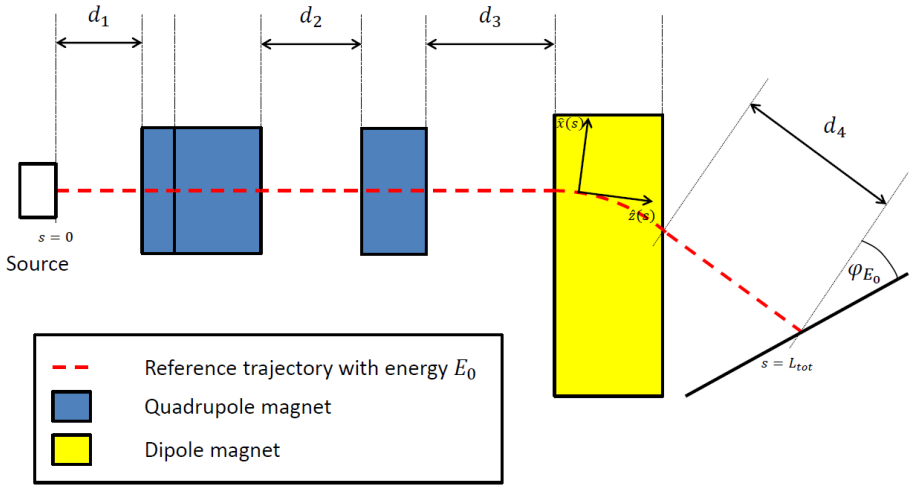

Figure 11: Layout of quadrupole triplet and dipole spectrometer beamline.

This spectrometer consists of three quadrupole magnets and a dipole magnet. The purpose of the triplet is to minimize the influence of the divergence and pointing fluctuations on the energy measurement. As with only the dipole (section 4.1) the screen is tiled by an energy dependent angle φ_{E_0}. The change of angle is only due to the change of reference particle trajectory. The calculation on how the angle changes with E_0 can be found in the APPENDIX 7.2. In the laboratory frame the angle φ of the screen remains constant. In the following section the optimal angle of the screen is calculated.

Under the special condition of a fixed distance d_4 and setup length L_{tot}

$$L_{tot}(E_0 \to \infty) = \text{const}$$
$$d_4(E_0 \to \infty) = \text{const},$$

the distances d_1, d_2 and d_3 can be calculated. By numerically solving the focus equations 2.1.6 and 2.1.7, the quadrupole magnet distances d_1, d_2 and d_3 can be expressed as functions of $L_{tot}(E_0 \to \infty)$ and $d_4(E_0 \to \infty)$. The optimal angle of the screen in these configuration is given by equation 2.1.8. For highly energetic electrons ($R \gg L_{di}$) it can be shown that the screen angle φ approaches $\pi/2$. Therefore it only makes sense to tilt the screen for energies ($R \approx L_{di}$). In the following we will only consider the case of a screen parallel to the dipole.

4.3.1 Resolution

As described in section 2.1.2 one can define the calibration curve $a(\delta)$ and the error of the spectrometer $\Delta E/E$. The resolution is maximal if the stigmatic focusing conditions (eq. 2.1.6, 2.1.7) hold for a energy E_0. By changing d_1 and d_2 one can tune the setup to have best resolution at specific energies E_0. Compared to the dipole spectrometer this

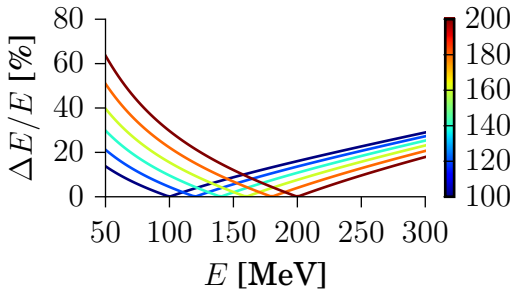

(a) Resolution of spectrometer for beam with $x' = 0$ and $\sigma(x') = 3\,\text{mrad}$.

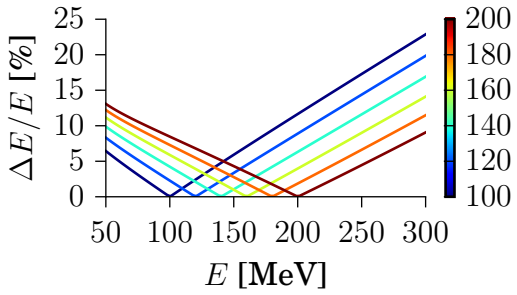

(b) Resolution of spectrometer for beam with $x' = 10\,\text{mrad}$ and $\sigma(x') = 3\,\text{mrad}$.

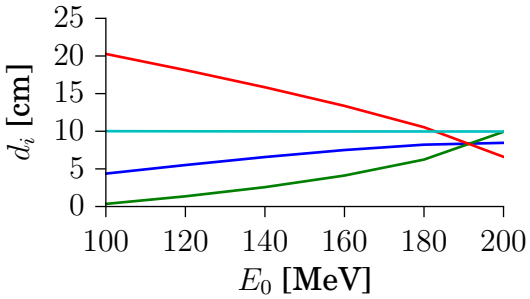

Figure 12: d_1 (blue), d_2 (green), d_3 (red), d_4 (cyan).

setup reaches better resolution around E_0. For energies lower than E_0 the effect of the quadrupoles leads to a worse resolution. For energies much higher than E_0 the resolution approaches the one of the dipole setup. Therefore such a setup should only be applied

if the energies of the beams are of the order of E_0 or above. The best configuration of this spectrometer can be reached if the dispersion of the dipole is combined with the dispersion of the quadrupoles under an angle $\bar{x}'$. Figure 12 shows that the resolution can be nearly doubled in a reasonable case. Especially for low energy electrons (below E_0) it can be improved significantly. Using a deviated beam has also the great advantage that the spectrometers acceptance with respect to pointing fluctuations rises. In the following section we are going to discuss the effect of negative x' on the monotonicity of the calibration curve.

4.3.2 False Peak in Energy Distribution due to Beam Pointing

A major problem of a this kind of spectrometer is that the calibration curve doesn't stay strictly monotonic (bijective) if the beam is deviated in the negative x-direction due to pointing fluctuations. This leads to Jacobian peaks in the final distribution on the screen which can be misinterpreted as peaked energy distributions. For low energies the

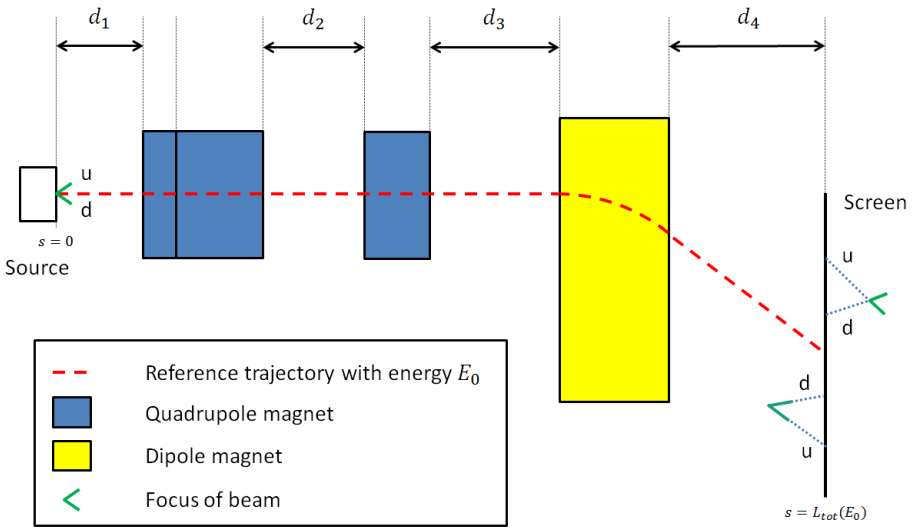

Figure 13: This picture illustrates how pointing fluctuations in the d-direction (negative x) can generate peaked distributions on the screen.

role of the triplet becomes more important. This means that for low energetic electrons with strong pointing fluctuations (here $E = 60\,\text{MeV}$ and $x' = -10\,\text{mrad}$) the effect of over-focusing is more relevant than the actual dispersion and the particle bunch would appear to have a peaked distribution reaching in high energies.

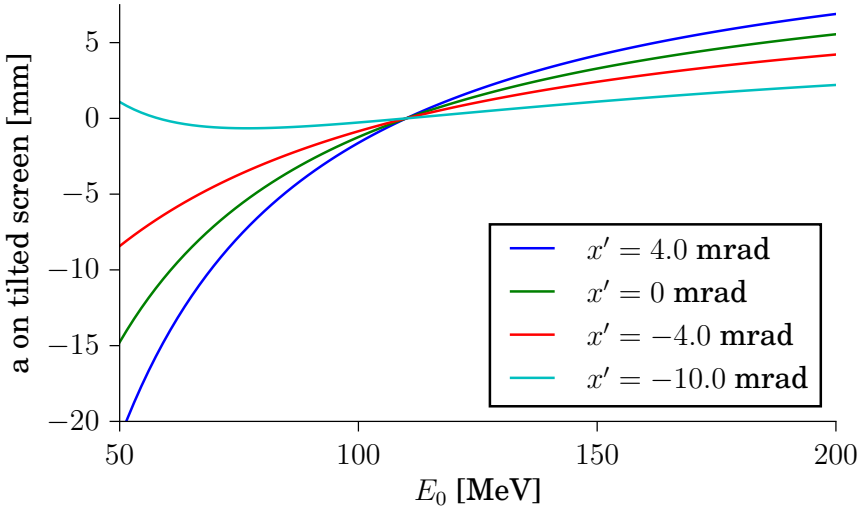

Figure 14: Position on screen as a function of energy E for different beam divergences x'.

5 Experimental Test of Spectrometer

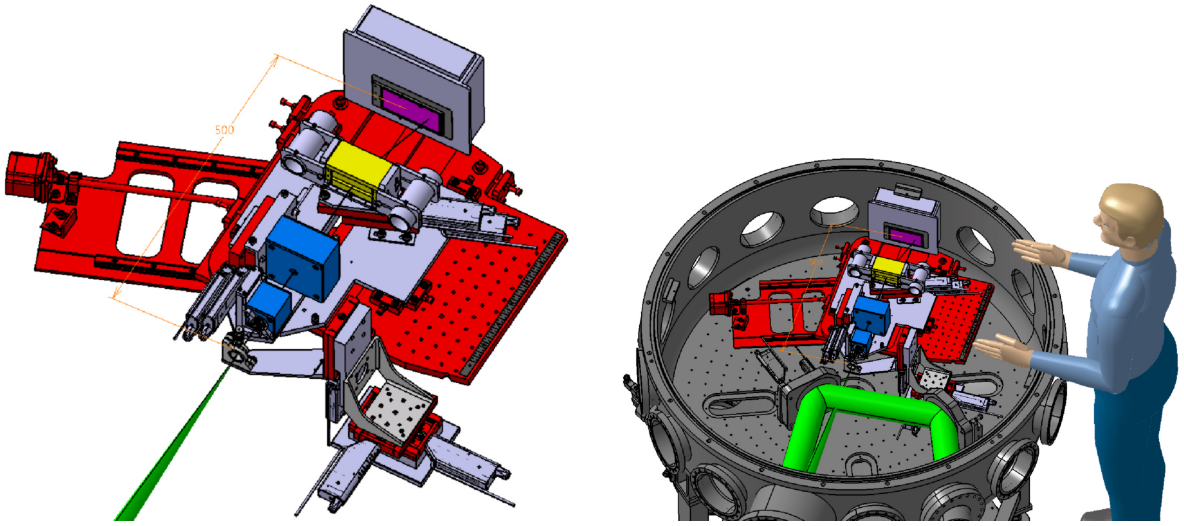

Figure 15: The images show the experimental setup installed in UHI100. The quadrupole magnets (blue) can be displaced by the linear stages (red). Also the dipole (yellow) can be moved out of the beam (green). The electron positions are measured on the screen (purple) which can be removed under vacuum to analyze the laser beam profile.

Using existing quadrupoles and a dipole magnet the design of the setup is thought to resemble all the above presented spectrometers (section 4). In addition all the electron optics can also be moved out to measure the beam fluctuations $\sigma\bar{x}'$ and divergence $\sigma x'$. The whole spectrometer is mounted on a aluminum plate which is fixed on a large translation stage. The first quadrupole which is actually a doublet, can be moved over a range of 50 mm. Relative to that we can translate the large quadrupole by 100 mm. This gives us the possibility to cover all the configurations show in figure 12. In other

words this means that the spectrometer is designed for a energy range form 100 MeV to 200 MeV. If the quadruple triplet is moved out of the beam by the large stage, we have the possibility to move in the dipole using a stack of two translation stages with a travel range of 50 mm (Dipole Spectrometer). In case the dipole is not in use (Pointing Measurement, Quadrupole Triplet Spectrometer) the dipole is move in a position such that the beam passes though one of the two soft iron tubes. These tubes have the purpose to shield the beam against the strong fringe field of the dipole magnet. For the quadrupole magnets such a protection was not necessary since there fringe field is very small due to better designed soft iron yokes in the magnet's casting. Another special feature of the setup is the under vacuum removable screen which enables direct vision of the laser pulse under vacuum. This is especially helpful when analyzing the experimental results. Tt determines the deviation of the laser axis with respect to the quadrupole axis. Also it offers to check whether the electron exit the source parallelly which should be the case for an ideal source. In the following sections we are going to discuss the alignment strategies and present some selected spectra measured by the different spectrometer configurations.

5.1 Alignment Strategies

A great challenge of the experiment was to align the laser, quadrupole and translation axis with each other. The alignment is divided in tree steps. The first two concern the alignment of the axis of translation with the axis through the centers of the quadrupoles and dipole. The third step concerns the alignment of the spectrometer with the electron source. This can only be done in the vacuum chamber (CEA) whereas the previous two steps have been done in the laboratories of LLR.

Mechanical Alignment of Translation Stages The setup was mounted on a CNC machine equipped with a micrometer indicator. Since all stages have to displace in the same direction (z), we can align them by displacing them manually while measuring the deviations in the two orthogonal directions (y, z). The precision of the alignment was however not limed by the precision of the indicator but by the deformation of the stages due to gravitational torque. The error of alignment therefore was 0.1 mm over a length of 5 cm (2 mrad).

Figure 16: Photo of mechanical alignment.

Laser Alignment of Magnetic Axis with Translation After the mechanical alignment the translation stages were co-moving up to a precision of 2 mrad. The axis of the quadrupoles and dipole however did not agree with each other to the same precision. We therefore placed the setup on an optical table. Before irises were mounded on the faces of the quadrupole magnets such that their centers agreed with the mechanical axis. A strongly attenuated HeNe laser which was cut by an iris to generate diffraction rings

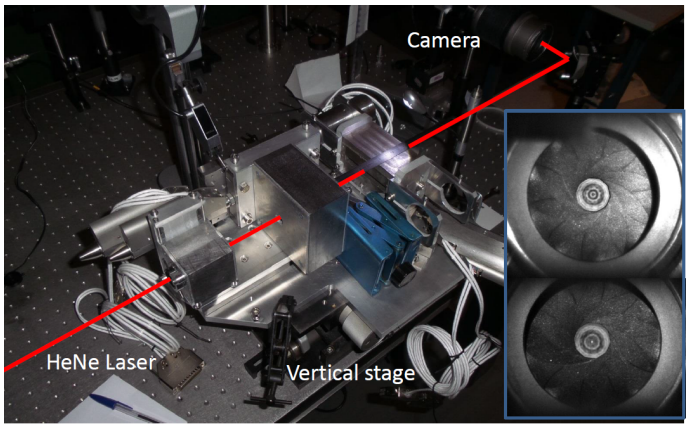

Figure 17: Photo taken while laser alignment The images in the blue frame show samples from the data taken with the camera. There are choses to show the maximal deviations.

was first centered on the large quadrupole at two different translation points. This was our reference to further align the the small quadrupole and the dipole with the HeNe. The precision was again limited by the deformation of the translational stages due to gravitational torque.

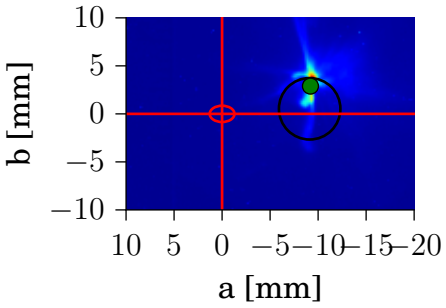

Figure 18: The images show how the alignment of the setup was done. In red we see the center of the electron beam on the screen when no magnetic elements are inserted. The laser is the black circle. The electron beam is centered on the green dot by the quadrupole triplet. This dot agrees horizontally with the laser. Vertically there is a discrepancy of about 3 mm. This is probably due to the strong magnification in the b direction of the triplet (factor 10). This means a misalignment of the source of about 0.3 mm. This value lies in the precision of the alignment method of using 2 irises.

5.2 Results

Here we will present some spectra measured by the device described in the beginning of section 5. For this report I pricked the most illustrating images. Because of instability of the source not all spectra are as nice. Since the aim of the experiment was to characterize the spectrometer and not the beam the last plot (Figure 22) is very important. For high energies there is a disagreement with the measurement and the peak of the distribution. This can be due to many things. In order to have a peak at the focus the energies of the beam must be high enough. Which is not the case (see Spectra). There could also be a problem with the model of the quadrupole triplet. Further analysis should characterize the field map and fit the best linear model to it (analogous to section 3).

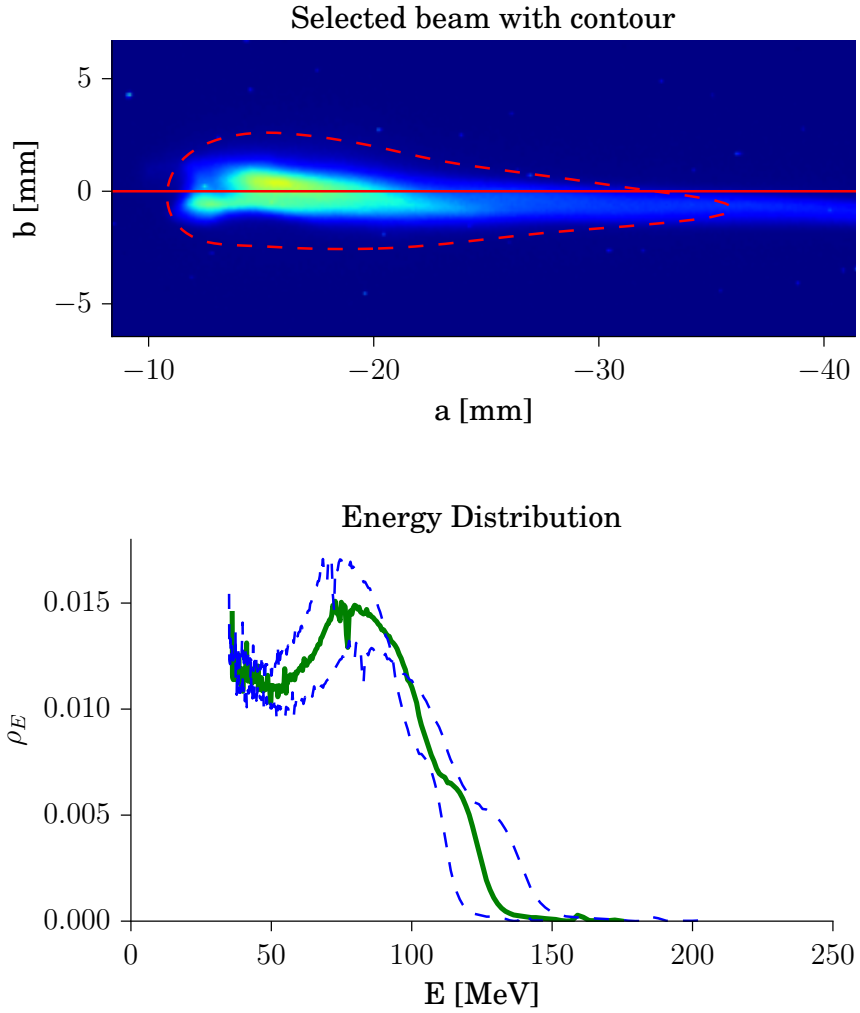

Figure 19: Energy distribution measured with a Dipole. The green distribution assumes a straight traveling beam. The blue lines show the two possible energy distribution under a pointing fluctuation of one standard deviation in x. The energy of the particle bunch reaches up to $(130 \pm 20)\,\mathrm{MeV}$ and is peaked at $(90 \pm 10)\,\mathrm{MeV}$. Note that the distribution ρ_E decreases almost monoconically between 100 MeV and 130 MeV.

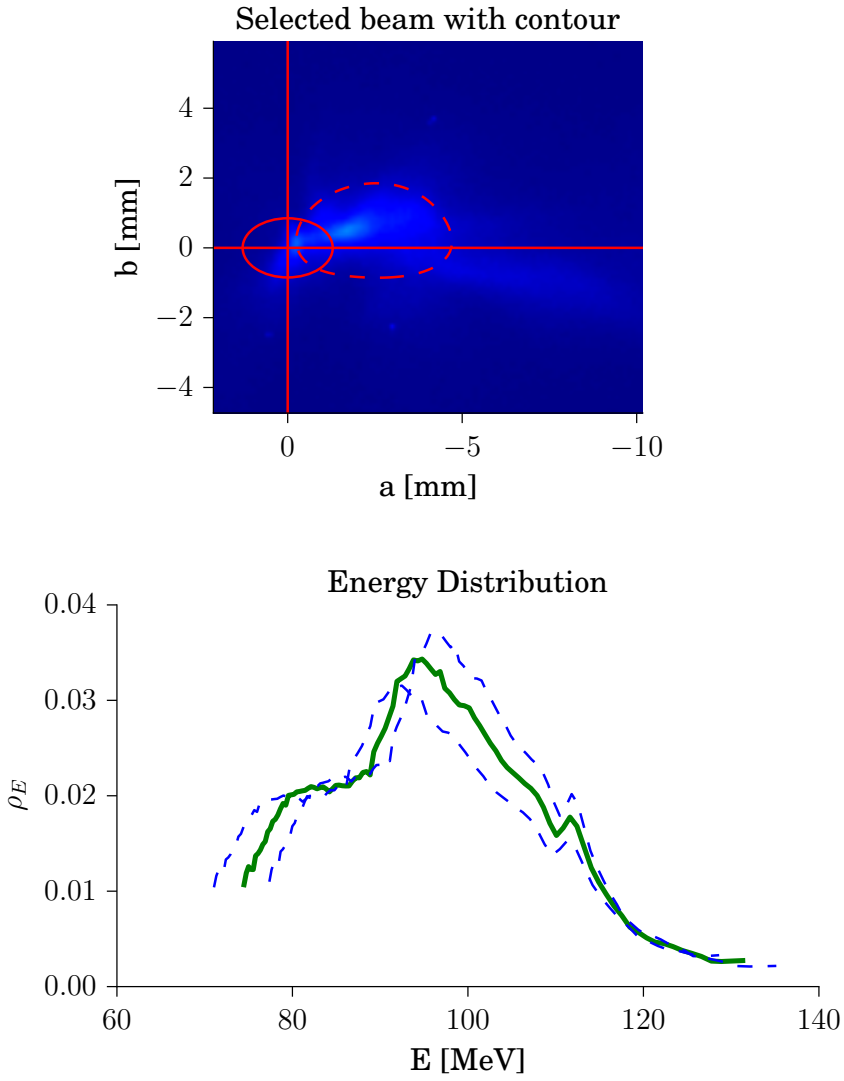

Figure 20: Energy distribution measured with a Quadrupole Triplet. The green distribution assumes a straight traveling beam. The blue lines show the two possible energy distribution under a pointing fluctuation of one standard deviation in x. Similar to the distribution measured by the dipole spectrometer the energy decreases almost linearly between 100 MeV and 130 MeV. We can see in both distributions a small kink at about 115 MeV. In the dipole spectrometer this kink is however smeared out because of the convolution with the beam deviation (lower resolution).

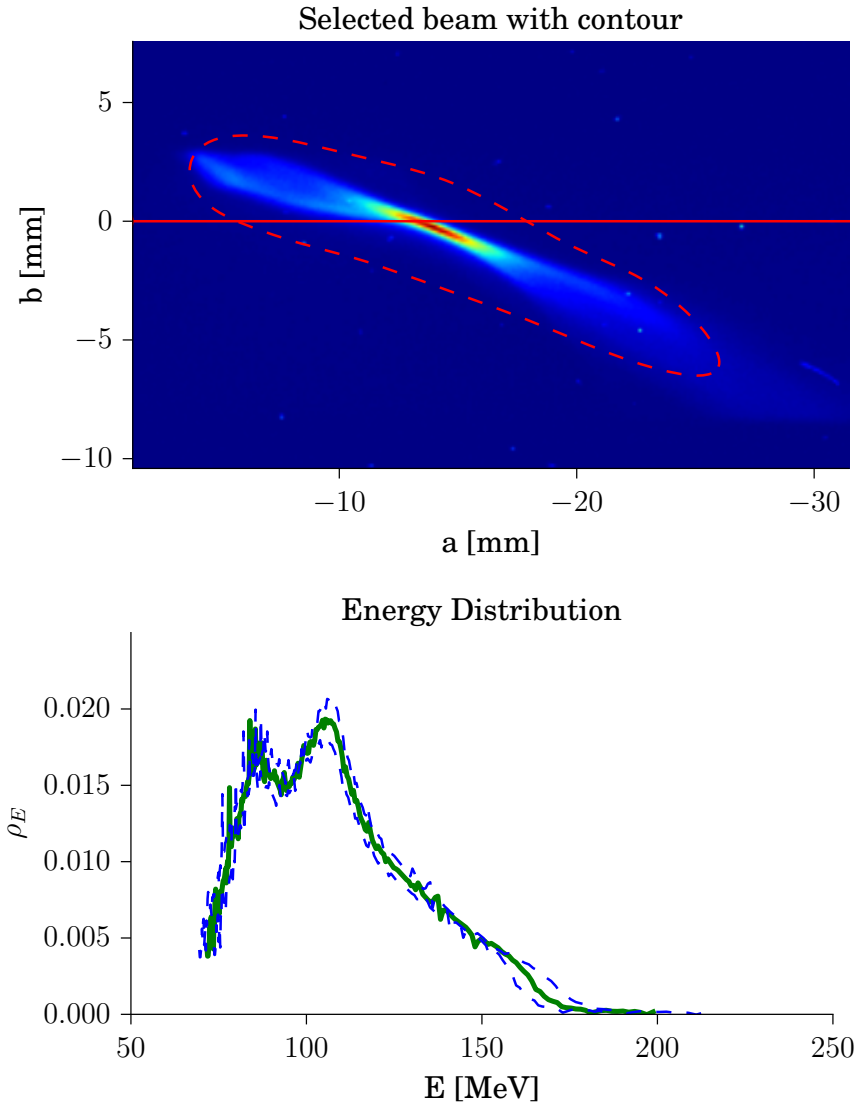

Figure 21: Energy distribution measured with a Quadrupole Triplet and Dipole Spectrometer. The green distribution assumes a straight traveling beam. The blue lines show the two possible energy distribution under a pointing fluctuation of one standard deviation in x. The image shows a nice example of the expected 'butterfly' distribution. One can see the focus point of the quadrupoles. The rotation of the butterfly is due to a pointing in the positive x direction. Compared to the other two spectrometers we see a high energy resolution over a large range. This is a result of the combination of the dispersion of the quadrupoles with the dipole.

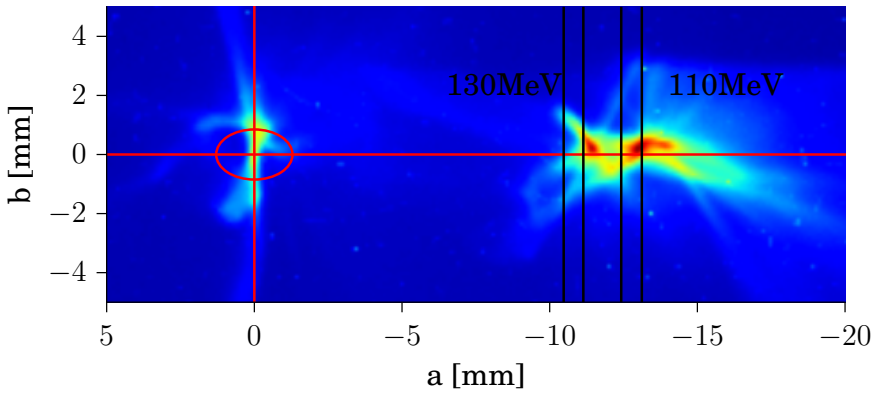

Figure 22: The image shows the sum over all shots without dipole (red cross) and with the dipole (black lines). The quadrupoles where then tuned to generate stigmatic focusing at 110 MeV and 130 MeV. Since the gradients of the quadrupoles where not known during the experiment, there was a small astigmatism in the image. The black lines in the plots show where the vertical and horizontal focus should be. This has been calculated after the gradients where know down to a percent level. For 130 MeV the peak doesn't agree with the simulation result. This can be due to alignment or the modeling of the quadrupole triplet.

6 Further Improvements and Outlook

Based on the results of the experiments we come to the conclusion that the spectrometer should be further characterized. Figure 22 indicates that the model applied to the quadrupoles in not perfectly describing our results. Since we only had effectively one day to take usable data, it was not possible to find the cause of the deviation. For further experiments I would suggest to scan more configurations of the spectrometer, for example 110 MeV to 150 MeV stigmatic in 10 steps. Using this data one would be able to fit more parameters of the model.

Additionally one would also have to quantify the errors of the theory better. It needs to be able to answer questions like: What is the error of the linear model? How will errors on the alignment modify the characteristics of the experiment? At what distance between the quadrupoles does the linear approximation fail (Fringe Field effects)? All these analysis could be done by combining the analytical calculations using `sympy` with the `uncertainties` package in `python` and performing an analysis similar to the one presented in section 3 also for the quadrupole triplet. Unfortunately there was not enough time in the internship to do this.

As described in section 5.1 the quadrupoles turned when translated due to the gravitational torque. In order to improve the model either the setup must be either constructed more rigid or the misalignment should be characterized as a function of the displacement of the stages.

7 APPENDIX

7.1 Maps of Elements

Drift Hamiltonian:

$$H = \frac{\delta}{\beta_0} + D\sqrt{1 - \frac{\hat{p}_x^2}{D^2} + \frac{\hat{p}_y^2}{D^2}} \approx \left(\frac{\delta}{\beta_0} - D\right) + \frac{\hat{p}_x^2}{2D} + \frac{\hat{p}_y^2}{2D} \tag{7.1.1}$$

Matrix:

$$\mathbf{M}_d = \begin{pmatrix} 1 & \frac{L}{D} & & & & \\ & 1 & & & & \\ & & 1 & \frac{L}{D} & & \\ & & & 1 & & \\ & & & & 1 & \\ & & & & & 1 \end{pmatrix} \tag{7.1.2}$$

Energy shift:

$$\mathbf{v}_d = \begin{pmatrix} 0 \\ 0 \\ 0 \\ 0 \\ 0 \\ \left[\frac{1}{\beta_0} - \frac{1}{D}\left(\frac{1}{\beta_0} + \delta\right)\right] L \end{pmatrix} \tag{7.1.3}$$

Dipole Hamiltonian:

$$H = \frac{\delta}{\beta_0} + (1 + k_0 x) D\sqrt{1 - \frac{\hat{p}_x^2}{D^2} + \frac{\hat{p}_y^2}{D^2}} + (1 + k_0 x) k_0 \left(x - \frac{k_0 x^2}{2(1 + k_0 x)}\right) \tag{7.1.4}$$

$$\approx \underbrace{\left(\frac{\delta}{\beta_0} - D\right)}_{\text{drift}} + \underbrace{k_0(1 - D)x}_{\text{dispersion}} + \underbrace{\frac{k_0^2}{2}x^2}_{\text{geometical focusing}} + \frac{\hat{p}_x^2}{2D} + \frac{\hat{p}_y^2}{2D} \tag{7.1.5}$$

Matrix:

$$\mathbf{M}_{di} = \begin{pmatrix} \cos(\omega L) & \frac{1}{\omega D}\sin(\omega L) & & & & \\ -\omega D \sin(\omega L) & \cos(\omega L) & & & & \\ & & 1 & \frac{L}{D} & & \\ & & & 1 & & \\ \mathbf{M}_{51} & & \mathbf{M}_{52} & & & 1 \end{pmatrix} \tag{7.1.6}$$

$$\mathbf{M}_{51} = \frac{1}{\sqrt{D}}\left(\frac{1}{\beta_0} + \delta\right)\left[-\sin(\omega L) + \frac{1}{2}\frac{D-1}{D}\left(\omega L - \frac{1}{2}\sin(2\omega L)\right)\right] \tag{7.1.7}$$

$$\mathbf{M}_{52} = \frac{1}{\omega D}\,\frac{1}{\sqrt{D}}\left(\frac{1}{\beta_0} + \delta\right)\left[\cos(\omega L) - 1 + \frac{1}{2}\frac{D-1}{D}\left(\cos^2(\omega L) - 1\right)\right] \tag{7.1.8}$$

Energy shift:

$$\mathbf{v}_{di} = \begin{pmatrix} (D-1)/k_0(1-\cos(\omega L)) \\ \omega D(D-1)/k_0 \sin(\omega L) \\ 0 \\ 0 \\ 0 \\ \mathbf{v}_z \end{pmatrix} \tag{7.1.9}$$

where $k_0 = \frac{q}{P_0}B_0$, $\omega = \frac{k_0}{\sqrt{D}}$ and $d = \frac{1}{\beta_0} - \frac{1}{D}\left(\frac{1}{\beta_0} + \delta\right)$

$$\mathbf{v}_z = dL - \frac{1}{\omega}\frac{D-1}{D}\left(\frac{1}{\beta_0} + \delta\right)\left[\omega L - \sin(\omega L) + \frac{1}{4}\frac{D-1}{D}\left(\omega L - \sin(2\omega L)\right)\right] \tag{7.1.10}$$

Quadrupole Hamiltonian:

$$H = \frac{\delta}{\beta_0} + D\sqrt{1 - \frac{\hat{p}_x^2}{D^2} + \frac{\hat{p}_y^2}{D^2}} + k_1(x^2 - y^2) \approx \left(\frac{\delta}{\beta_0} - D\right) + \frac{\hat{p}_x^2}{2D} + \frac{\hat{p}_y^2}{2D} + k_1(x^2 - y^2) \tag{7.1.11}$$

Matrix:

$$\mathbf{M}_{qp} = \begin{pmatrix} \cos(\omega L) & \frac{1}{\omega D}\sin(\omega L) & & & \\ -\omega D \sin(\omega L) & \cos(\omega L) & & & \\ & & \cosh(\omega L) & \frac{1}{\omega D}\sinh(\omega L) & \\ & & \omega D \sinh(\omega L) & \cosh(\omega L) & \\ & & & & 1 \end{pmatrix} \tag{7.1.12}$$

Energy shift:

$$\mathbf{v}_{qp} = \begin{pmatrix} 0 \\ 0 \\ 0 \\ 0 \\ 0 \\ \left[\frac{1}{\beta_0} - \frac{1}{D}\left(\frac{1}{\beta_0} + \delta\right)\right] L \end{pmatrix} \tag{7.1.13}$$

where $k_1 = \frac{q}{P_0}g$, $\omega = \sqrt{\frac{k_1}{D}}$ and g is the gradient.

7.2 Change of Reference Energy E_0 in Dipole

The use Frenet-Serret coordinates to describe dipoles introduces a nontrivial transformation of the particles coordinates under the change of E_0.

The screen defining coordinates $d_2(E_0)$ and φ_{E_0} (figure 7, 23) transform like

$$d_2(E_1) = \frac{\cos(\vartheta_0)d_2(E_0) - \sin(\varphi)\Delta a_{01}}{\cos(\vartheta_1)} \tag{7.2.1}$$

$$\varphi_{E_1} = \varphi_{E_0} + \vartheta_0 - \vartheta_1 \tag{7.2.2}$$

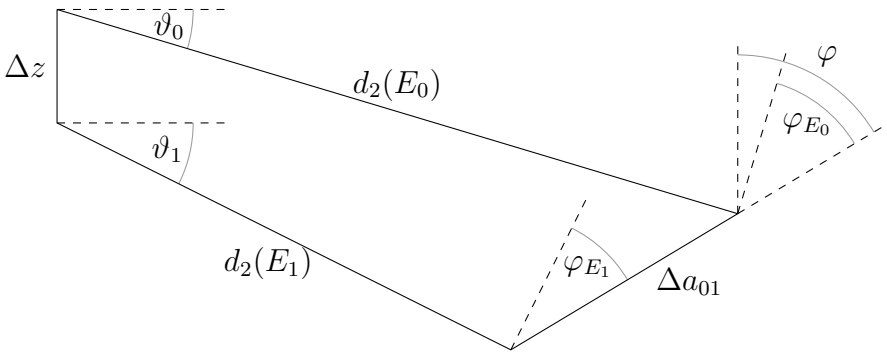

Figure 23: Sketch of reference trajectories after dipole. The termination of the coordinate transformation under change of reference energy from E_0 to E_1.

under the change of reference energy from E_0 to E_1. ϑ_0 and ϑ_1 are the angles of the reference particle exiting the dipole. They are given by

$$\vartheta_i = \arcsin\left(\frac{L_{di}}{R_i}\right),$$

$R_i = \frac{P_i}{eB}$ being the radius of curvature in the dipole of length L_{di}. The angle φ describes the tilt of the screen in the lab frame. It can be calculated by the transformation from E_0 to $E_1 \to \infty$.

$$\varphi = \varphi_{E_0} + \vartheta_0$$

The z coordinate of the reference particle exiting the dipole in the laboratory frame changes by

$$\Delta z = R_0(1 - \sqrt{1 - (L_{di}/R_0)^2}) - R_1(1 - \sqrt{1 - (L_{di}/R_1)^2}).$$

The screen coordinates are shifted by $a_1 = a_0 + \Delta a_{01}$ and $b_1 = b_0 + \Delta b_{01}$, where

$$\Delta a_{01} = \frac{\Delta z + d_2(E_0)\left(\tan(\vartheta_1) - \cos(\vartheta_0) - \sin(\vartheta_0)\right)}{\cos(\varphi) + \tan(\vartheta_1)\sin(\varphi)}$$
$$\Delta b_{01} = 0.$$

7.3 Manual for SpectroAnalyser

The task of the program is to track particle bunches through beamlines. It makes use of the 6D linear model. It gives the possibility to look at particle bunches at all positions s of the beamline using a slider. The user just has to change the parameters in the `main.py` file. The example should be self-explanatory

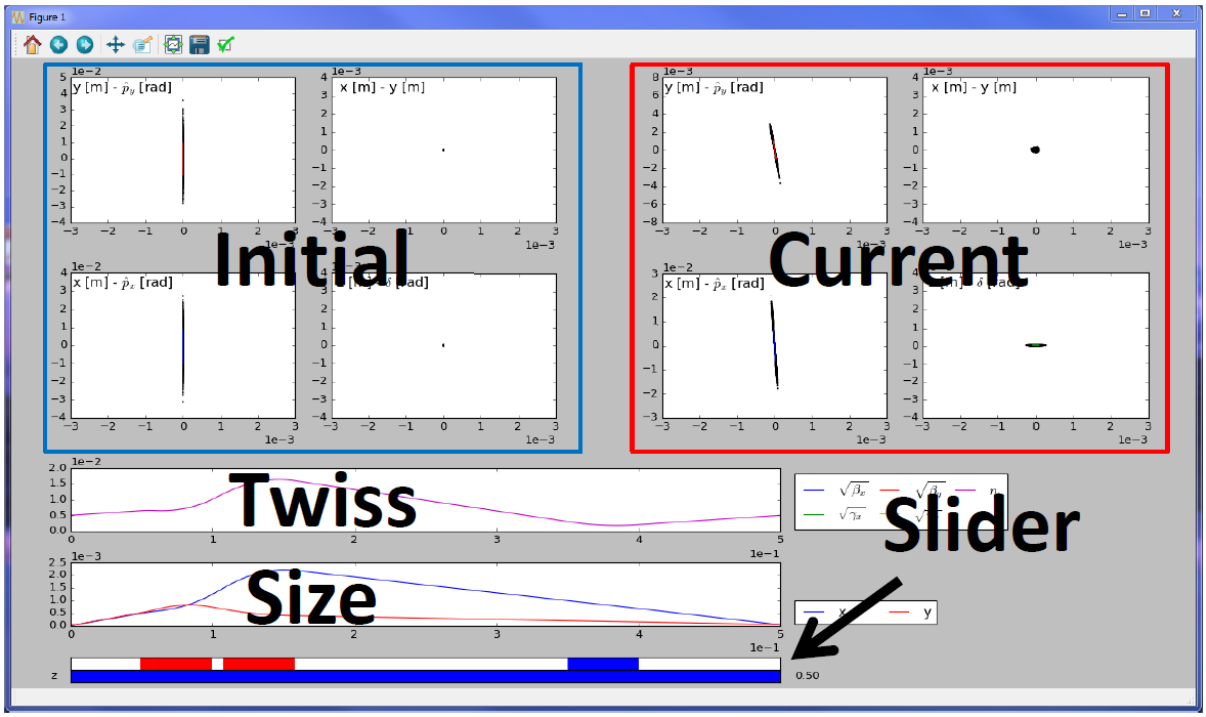

7.4 Manual for LinearModelTracker

The program has been entirely written for `python 3.5`. In order to run the program I recommend to install anaconda python 3.5 which can be downloaded here: https://www.continuum.io/downloads. The program consits of two different sections. First there is the folder scrips where all the `.py` scripts are located. These scripts contain most of the classes and functions in order to describe the models and analysis described in this report. The second folder contains `jupyter` notebooks. These notebooks contain examples of how the scripts can be used to describe a spectrometer. The python scrips are called by the notebooks. The advantage of using notebooks is that text and images can be included to further illustrate the code. The following subsections have the purpose to link the python scripts and notebooks to the ideas presented in this report.

7.4.1 Semi-Linear Model

`LinearModel_Accelerator.py`, `LinearModel_Elements.py` These two scripts implement the linear model described in section 2.1. The elements of APPENDIX 7.1 are included in `LinearModel_Elements.py`. The main idea is to create an `accelerator` object (`acc = accelerator(E0, parameters, list_of_elements)`) that contains the reference energy E_0, the elements and some parameters (array of `sympy` symbols). In the case of a quadrupole and dipole spectrometer these parameters would be the distances between the elements d_i. However one can choose arbitrary parameters. The `accelerator` object offers then the possibility to analytically calculated quantities like the derivatives of the matrix elements with respect to the energies δ (for example `acc.dmatrix`). If a specific configuration of the parameters is fixed (`acc.set_config(config)`) these quantities can be calculated fast as a function of delta (for example `acc.dmatrixfc(delta)`), where c stands for config fixed and f for function of *delta*. Additionally to that the class also implements functions that offer to show a beam on the screen with angle ϕ to the reference trajectory (`acc.plot_contours_on_screen`) or calculate the resolution of an spectrometer (`acc.deltav_er(dxp , deltav, phi)`). Later is a direct implementation of formula 2.1.5.

`ReferenceTrajectories.py` This script implements a method `push(list_of_elements, sa, r0 , phi0)` to get the lab coordinates of reference particle with energy E_0 that traveled a distance `sa`. The elements are also defined in the same script. For the future it would be nice to combine this feature with the elements defined in `LinearModel_Elements.py`.

`VariableSpectrometer.py` The most important functions in the script are `d1d2d3(acc, d4v, L_totv, deltav, focus = 'stigmatic', deltavx = None, deltavy = None)` and `angle_of_DFP(acc, d4v, L_totv, deltav)` which find the focusing conditions (section 2.1.3) numerically and find the optimal angle of the screen for best resolution (section 2.1.4). Other functions are `plot_er(acc, deltamin, deltamax, phi, dxp ,absolute = False, linewidth = 1, figure = True, color = None)` that plots the error curve like in figure 10. One can also show the configuration of the build spectrometer using `plot_spectrometer(d1v ,d2v ,d3v ,d4v ,phi_ref ,E0a ,L_qu , L_di, B)`.

ChangeOfE0.py Like the name of the script tells it directly implements the ideas of APPENDIX 7.2. This is needed when changing between the co-moving and lab frame.

7.4.2 Field Maps and Tracking

This part of the program deals with modeling a dipole (section 3).

FieldMaps.py This script can show some plots of the field of a dipole that has been measured using the LLR field map scanner. And for the map of B_z calculate all the other field components. The field map object can be initialized using `fm = fieldmap(filename, dx, dy, dz, field_direction = 'z')`. The field can be read out with `fm.B(x, y, z)`

FieldMapTracking.py Using a field map obejct one can define an accelerator object by `acc = accelerator(B, E0)`, where B must be a function of x, y and z. The trajectories of electrons in the field B can be calculated by `acc.track( T, x, ux, y, uy, z, uz, n = 1000)`. Another important feature is the `get_matrix(E0, delta, trackfun, dxiv = 1e-6)` function which calculates the accelerator matrix of the linear model using equation 3.2.

7.4.3 Image Processing and Experimental Analysis

The last part of the software is the analysis of images of the screen using the methods described in section 2.2.

ImageProcessing.py (Image → Distribution on Screen) This script reads and analyses distributions of the screen using `skimage`. It can detect partible bunches (`find_peak( im, plot = False,threshold = 0.25, max_sigma=30)`), calibrate the scale of the image (`calibration(file, x1, x2, y1, y2, plot = False)`) and calculate the energy distribution from the image (`get_energydistribution(acc, file, ...)`). Note that this function needs an accelerator object that is defined in `LinearModel_Accelerator.py`.

Distribution.py (Distribution on Screen → Energy Distribution) This script deals with the unfolding of the distribution of the screen to an energy distribution. The most important functions are first `get_energy_distribution(...)` to get the energy distribution from a 2d screen distribution using the Fredholm Method, second `get_energy_distribution_projected(...)` in combination with `project_on_a(...)` to get the energy distribution based on a projection on the a axis (fredhold and trival method possible).

7.4.4 Additional Tools

NicePlots.py This script deals with the plots. It adjusts the format such that the font style and size are unified and look nice when included in a latex script (latexify(columns=1)).

Notation and Symbols

δ $= \frac{E-E_0}{P_0 c}$ energy diviation

λ $\in \mathbb{R}^6$ phase space coordiante

ρ_Q Distribution of Quantity Q

D $= \sqrt{1 + \frac{2\delta}{\beta_0} + \delta^2}$ momentum conversion factor

E_0 total energy of reference particle

P_0 momentum of reference particle

References

[1] Per Christian Hansen. *Rank-Deficient and Discrete Ill-Posed Problems: Numerical Aspects of Linear Inversion.* siam, 1998.

[2] K. Nakamura, W. Wan, N. Ybarrolaza, D. Syversrud, J. Wallig, and W. P. Leemans. Broadband single-shot electron spectrometer for GeV-class laser-plasma-based accelerators. *Review of Scientific Instruments*, 79(5):053301, may 2008.

[3] Christopher M. S. Sears, Sofia Benavides Cuevas, Ulrich Schramm, Karl Schmid, Alexander Buck, Dieter Habs, Ferenc Krausz, and Laszlo Veisz. A high resolution, broad energy acceptance spectrometer for laser wakefield acceleration experiments. *Review of Scientific Instruments*, 81(7):073304, jul 2010.

[4] Helmut Wiedemann. *Particle accelerator physics.* Springer, 2015.